Authors: Lakshminath Kundanati, Roberto Guarino, Michele Menegon, Nicola M. Pugno

A. Viper (*Bitis arietans*)

D. Burrower (*Atractaspis aterrima*)

©Tyrone Ping

Fang penetration and retraction during biting
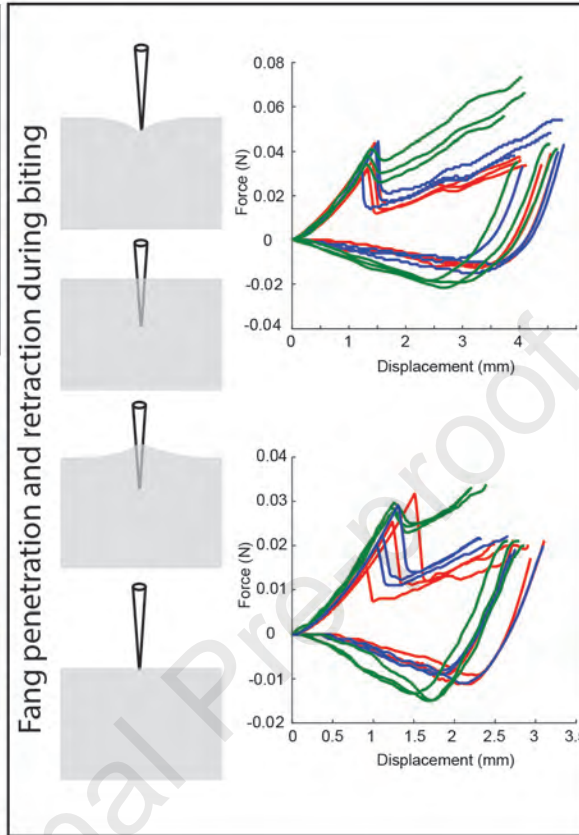
Nanoindenation : Young's modulus, hardness.
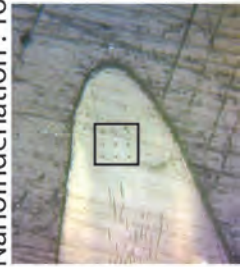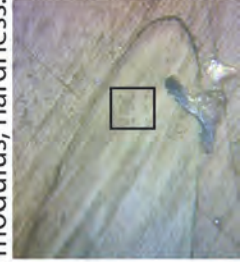
1 # Mechanics of snake biting: Experiments and Modelling

2 **Lakshminath Kundanati[1],[**], Roberto Guarino[1],[†],[**], Michele Menegon[2] and Nicola M.**

3 **Pugno[1],[3],[*]**

4

5 *[1] Laboratory of Bio-inspired, Bionic, Nano, Meta Materials & Mechanics, Department of*

6 *Civil, Environmental and Mechanical Engineering, University of Trento, via Mesiano 77,*

7 *I-38123 Trento, Italy.*

8 *[2] Division of Biology & Conservation Ecology, Manchester Metropolitan University, UK;*

9 *PAMS Foundation, P.O. Box 16556, Arusha, Tanzania.[3] School of Engineering and*

10 *Materials Science, Queen Mary University of London, Mile End Road, E1 4NS London,*

11 *United Kingdom.*

12 .

13

14 *[**] These authors contributed equally to this work*

15

16 * Corresponding Author:

17 nicola.pugno@unitn.it

18

19

20

21

22 *[†]* Present address:

23 *École Polytechnique Fédérale de Lausanne (EPFL), Swiss Plasma Center (SPC), CH-*

24 *5232 Villigen PSI, Switzerland*

25

26

27 ## Abstract

28

Among all the vertebrates, snakes possess the most sophisticated venom delivering system using their fangs. Fangs of many animals are well adapted to the mechanical loads experienced during the functions such as breaking the diet and puncturing the skin of the prey. Thus, investigation and modelling of puncturing mechanics of snakes is of importance to understand the form-function relationship of the fangs and tissue-fang interactions in detail. We have thus chosen fangs of two snake species i.e. viper (*Bitis arietans*) and burrowing snake (*Atractaspis aterrima*), with different shape and size, and performed insertion experiments using tissue phantoms. Our results showed that the fangs of both species have similar mechanical properties but there was a difference in the insertion forces owing to the difference in shape of the fang. Also, our modelling of the fang-tissue interactions predicted some material parameters close to the experimental values. Thus, our study can help in the development of bioinspired needles that can potentially have reduced insertion forces and less damage to the tissue.

1. Introduction

62   Biological structures like teeth are known to adapt well to mechanical loading conditions [1].

63   Among all the vertebrates, snakes possess the most sophisticated venom delivering system

64   using their fangs [2]. Fangs are the special teeth that are used to inject venom in to prey by

65   many species, using a venom canal that runs through [3]. Their long tubular fangs facilitate

66   injection of venom deep into the skin of the prey [4]. In order to cut through the prey tissue,

67   the material of the fang must be of similar or of stiffer material [5]. As mentioned, teeth and

68   fangs of many animals are well adapted to the mechanical loads experienced during the

69   function of either breaking the diet or puncturing the skin of the prey. Spider fang was

70   observed to have a design with fine mechanical tuning of properties at different locations for

71   easy piercing, reducing wear and withstanding stresses [5]. Changes in the shape and size of

72   the fang during evolution could have occurred also with the goal of injection system [6].

73   Investigating mechanics of puncturing by various snakes is of importance to understand the

74   form-function relationship of the fangs.

75   Understanding the tissue-fang interaction is important to get an overall idea of the

76   biomechanics of insertion during biting. There are many earlier studies which addressed the

77   needle-tissue interactions with the goal of designing needles that induce minimum pain [7,8].

78   Modelling of the forces involved in puncturing is done by separating the contributions

79   coming from the stiffness of the tissue or phantom material, the piercing force during the

80   initial phase of insertion and the frictional force at the interface of the needle the substrate

81   [9]. Most of these studies are based on standard suture needles or needles specially developed

82   for the percutaneous use. There are a very few studies which directly used a fang or a

83   piercing organ of an animal to study the interaction [10,11]. Using natural piercing organs

84   also present more challenges but the experiments helps in understanding the interaction in a

85   better way.

86   The goal of our study is threefold. Firstly, to perform piercing experiments on a substrate that

87   has material properties such as Young's modulus close to that of a human or an animal skin,

88   to understand the mechanics of fang insertion. Secondly, to determine the mechanical

89   properties of the fangs for comparison. Finally, to analytically model the insertion process at

90   various stages and fruther validate the model with the experimental data. We used fangs of

91   two snake species with fangs of different shape and size, respectively the Puff adder (Bitis

92   arietans) a large viperid snake, with long, hollow, articulated fangs which fold against the

93   roof of the mouth when the jaws are closed, mainly feeding on small mammals and birds and

94   with a bite that is considered a medical emergency in humans; and the Slender burrowing asp

95   (Atractaspis aterrima), a fossorial snake with relatively long fangs able to envenomate preys

96   with a unilateral backward stab of one fang projected from a partly open or closed mouth.

97   They have long fangs which can rotate and are hollow [12]. On the other hand, burrowing

98   snake has relatively shorter fangs and preys upon relatively small animals as compared to the

99   viper species. In order to understand the role of speed on the insertion force, we have

100   performed experiments at three piercing speeds. This study would help in understanding the

101   mechanics of fang insertion during biting and can also be extended to aid in the development

102   of needle design in biomedical applications.

103   **2.   Materials and Methods**

104   **2.1. Microscopy**

105   Images of the fangs are taken using an optical microscope (Lynx LM-1322, OLYMPUS) and

106   a CCD camera (Nikon) attached to the microscope. The dimensions from the optical images

107   are quantified using the standard calibration.

108   Scanning Electron Microscopy (SEM) was performed on the prepared fangs post mechanical

109   tests. They are carefully mounted on double-sided carbon tape, stuck on an aluminium stub

110   followed by sputter coating (Manual sputter coater, Agar scientific) with gold. A SEM (EVO

111   40 XVP, ZEISS, Germany) was used with accelerating voltages between 5 and 20 kV.

112   ImageJ software was used for all the dimensional quantification reported in this study [13].

113   **2.2. Gel preparation**

114   Food grade gelatine was used to make the phantom gels. The plate-like gelatine was broken

115   into pieces and measured in the weighing balance to mix right proportions (1 g gelatine in 5

116   ml of water). The pieces of gelatine were soaked in water for 10 minutes and later thoroughly

117   mixed in water with a temperature around 80°C. The gel was then poured in Teflon moulds

118   for curing and later placed inside a refrigerator for gelation. The cured gels were carefully

119   taken out of the moulds and used for experiments.

120   2.3. **Compression testing**

121   We have estimated the bulk mechanical properties of the gelatine hydrogels using rectangular

122   blocks (15 mm × 10 mm × 9.5 mm). We applied force on the gels (number of samples = 4)

123   using a flat platen at a rate of 0.01 mm/sec, using Messphysik MIDI 10 (MESSPHYSIK,

124   Germany) Universal Testing Machine and the forces were recorded using transducer of

125 (LEANE Corp., ±2 N). The initial linear region of the stress-strain curve is used to estimate

126 the Young's modulus of the material.

127 **2.4. Wire cutting**

128 We used wires of three different diameters (0.18, 0.4 and 0.8 mm) to determine the fracture

129 toughness of the gels (2 samples for each diameter) which are used in the piercing

130 experiments. The wires were kept taught between two points on the custom made set up and

131 are pushed in the gel along the width of the gel block. The gels used in these experiments

132 were prepared as mentioned in the corresponding section. The wires were pushed at a rate of

133 0.1 mm/s through the gels.

134 **2.5. Piercing force experiments**

135 The fangs were fixed in resin at the base of the fang to aid in holding the samples without

136 causing damage. Piercing experiments were performed using a Messphysik MIDI 10

137 (MESSPHYSIK, Germany) Universal Testing Machine and the forces are obtained using

138 transducer of (LEANE Corp., ±0.25N). Specimens (n = 3, at each rate) were pierced in

139 displacement-control mode at different rates (0.01, 0.1 and 1 mm/s) until the straight portion

140 of the fang was inserted into the gel. The various stages of gel deformation and needle

141 insertion and retraction are depicted in the schematic (Figure 1).

142

143 **2.6. Nanoindentation**

144 All fangs are embedded in a resin and polished using a series of 400, 800, 1200, 2000 and

145 4000 grade sand papers. Finally, the sample was polished using a diamond paste of particle

146 sizes in the range of 6 µm and 1 µm, to obtain a surface of minimal roughness. The material

147 properties of fangs are then determined using nanoindentation. We used Berkovich indenter

148 to perform nanoindentation experiments with a maximum load of 30 mN on the polished

149 cross-sectional surface of the tooth samples. We used a matrix format (3×3) to perform a total

150 of 18 indentations with 9 at each location with a prescribed distance between them. A

151 Poisson's ratio of 0.31 was used for estimating the Young's modulus.

152

153
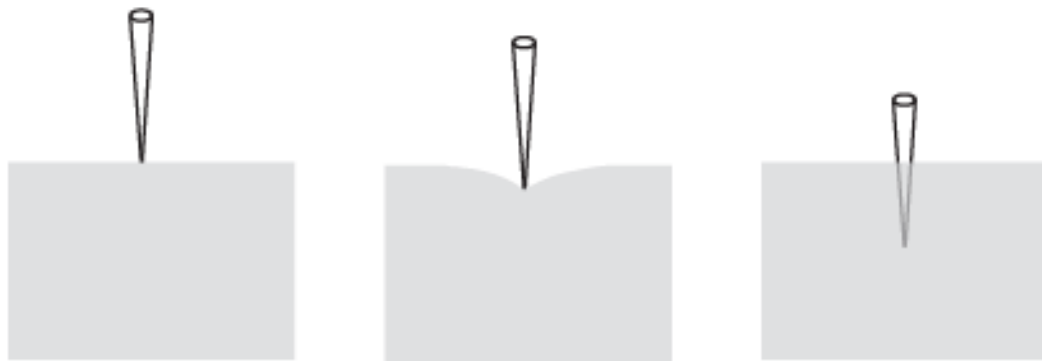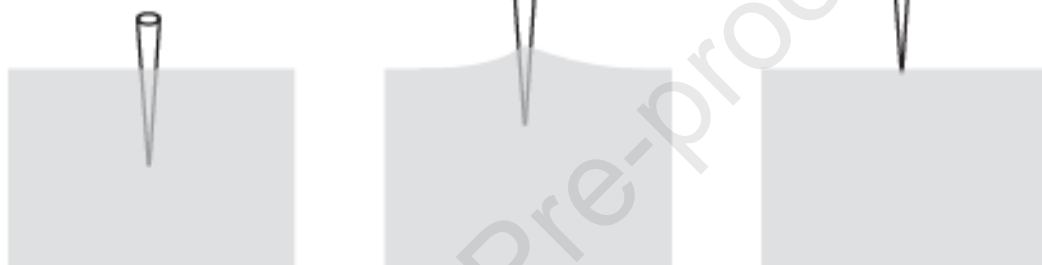
Figure 1. Different stages of needle movement during penetration and retraction.

3. Results and Discussion

3.1. Morphology and properties of fangs

The shape and tip morphology are determined to see their effects on the insertion force during the experiments of the two selection snake species, viper (*Bitis arietans*) and burrowing snake (*Atractaspis aterrima*) (Figure 2A & 2D). The optical images show that the fang of the viper is longer and has more curvature as compared to the burrower (Figure 2B & 2E). Scanning electron images of the fang tips show that the tip sharpness is almost similar in both the species (Figure 2C & 2F).

A. Viper (*Bitis arietans*) B. C.

D. Burrower (*Atractaspis aterrima*) E. F.

164
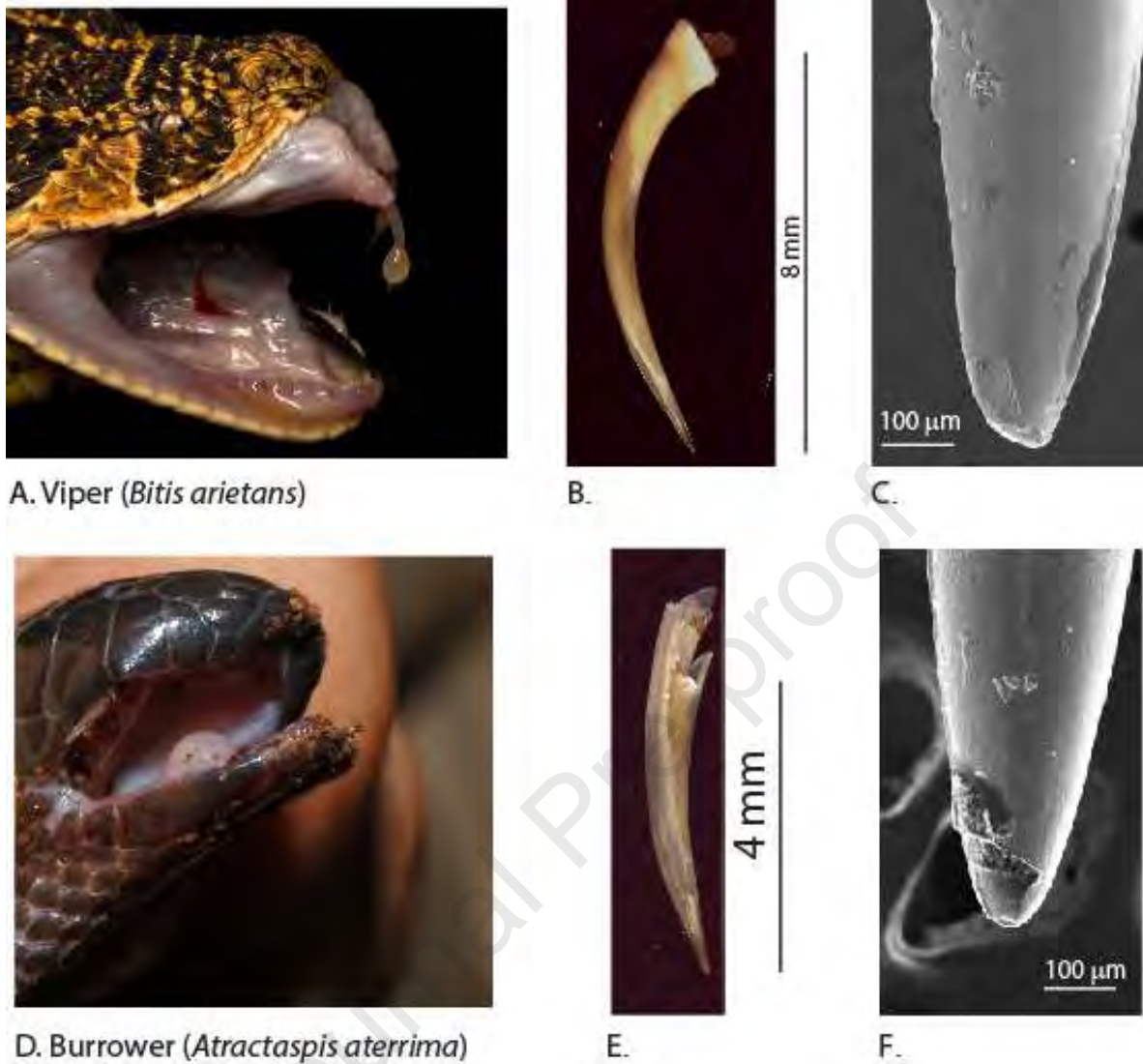
Figure 2. **Images of viper snake A.** head and mouth parts (Image: ©Tyrone Ping
(www.tyroneping.co.za)). **B.** Fang **C**. SEM image of it. **Images of burrower snake D**. head
and mouth parts **E**. Fang **F.** SEM image of it.

The mechanical properties of the fangs were determined by performing nanoindentation at
different locations on the polished sample surfaces (Figure 3). The measured elastic modulus
and hardness of the fangs of the burrower and viper are found to be similar (Table 1). There
are no significant differences in the measured properties at the tip region and the base region
of the fang. These values are in agreement with the reported values of Young's modulus
(15.3-24.6 GPa) of fangs of some snake species [14].

176   **Table 1**. Elastic modulus and hardness of the fangs

Sample	Region	Elastic modulus (GPa)	Hardness (GPa)
Viper	**Tip**	17.8 ± 2.3	0.71 ± 0.06
	Base	19.2 ± 0.4	0.75 ± 0.01
Burrower	**Tip**	18.9 ± 4.7	0.92 ± 0.05
	Base	18.7 ± 2.0	0.86 ± 0.03

177

A. Viper   A. Burrower

178

179   **Figure 3**. The indentation marks are clearly visible on the polished fang cross-sections of **A.**
180   Viper and **B**. Burrower.

181   **3.1.1. Compression testing and piercing testing**

182   The stress-strain curves from the compression testing of the gelatine hydrogels showed good
183   repeatability (Fig. 4). The Young's modulus of the gelatine hydrogels was measured to be
184   380 ± 65 kPa. Using gels of same composition, the force-displacement curves are obtained
185   from the piercing tests performed at different rates. The curves resembled standard piercing
186   tests with a linear increase in force with increase in displacement, followed by a sudden drop

187 in force and then a gradual increase (Fig. 5). Using the curves, the force and depth values at

188 the beginning of piercing are obtained and the values from tests at different piercing rates are

189 compared. We also measured the force value drop just after the initial piercing. The piercing

190 forces of burrowing snake fang are 23 ± 9, 23 ± 3 and 27 ± 1 mN for rates of insertion 0.01,

191 0.1 and 1 mm/s, respectively. The values of substrate surface deflection at the time of

192 piercing varied a bit. The piercing forces of viper snake fang are found to be 36 ± 6, 37 ± 8

193 and 37 ± 8 mN for rates of insertion 0.01, 0.1 and 1mm/sec respectively. In both the species,

194 the piercing force and substrate surface deflection at the time piercing did not vary

195 significantly with increase in speed of insertion. We also observed that the fangs experience a

196 negative pull while the fangs were being retracted because of frictional and adhesive effects

197 at the fang-gel interface (Fig. 5). The retraction forces were observed to be decrease with the

198 decrease in the speed of insertion (Table 2).
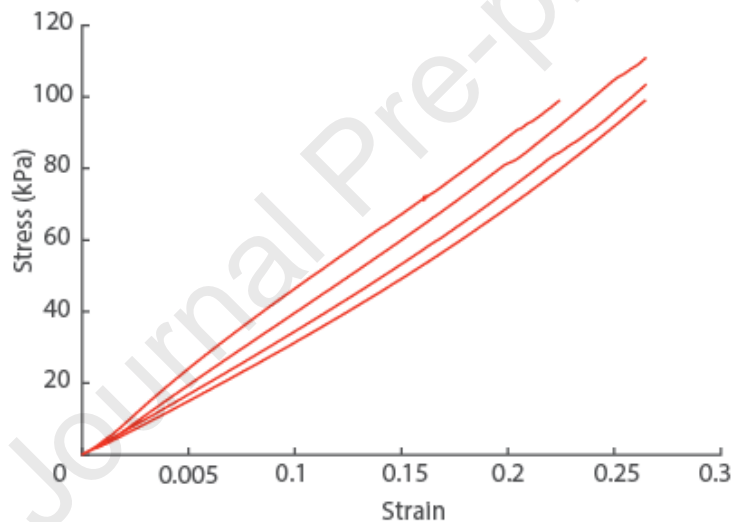
199

200 **Figure 4**. Stress-strain curves from the compression testing of the gelatine blocks.
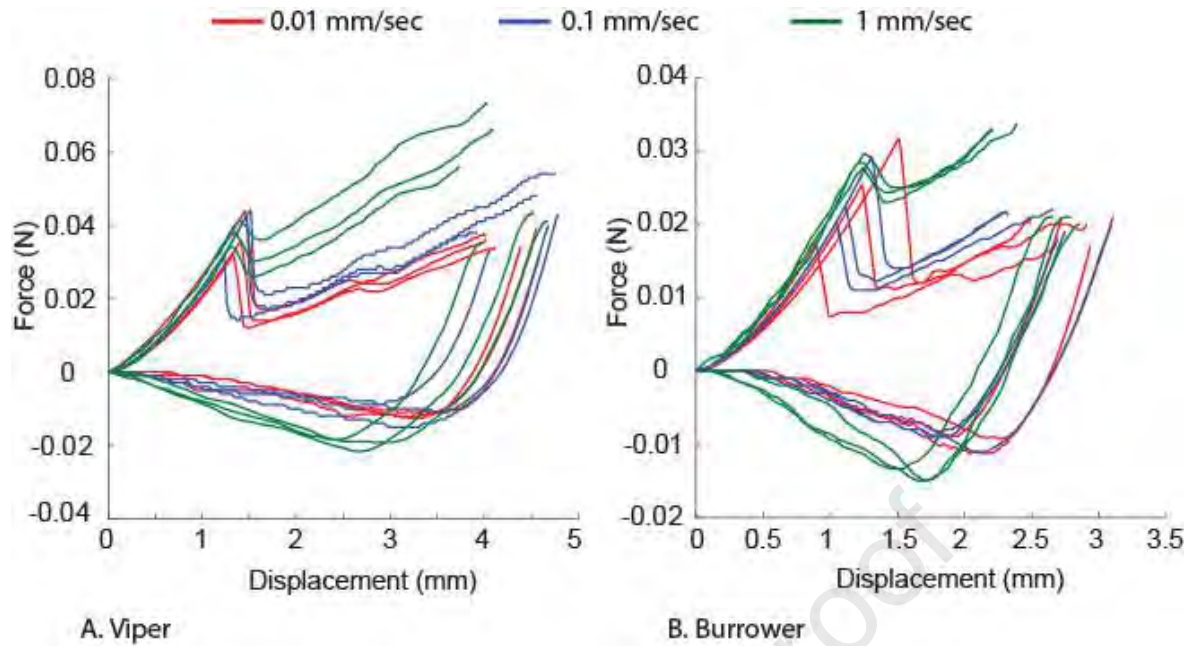
A. Viper   B. Burrower

Figure 5. Force-displacement curves during insertion and retraction tests performed at different rates. **A**. Viper **B.** Burrower snake.

Table 2. Piercing force of burrowing snake and Viper snake

	Insertion speed (mm/sec)	Piercing force (mN)	Deflection at piercing (mm)	Force drop (mN)	Retraction force (mN)
Burrower	0.01	23 ± 9	1.5 ± 0.4	24 ± 4	12.3 ± 1.5
	0.1	23 ± 3	1.1 ± 0.1	22 ± 4	12.6 ± 2.1
	1	27 ± 1	1.2 ± 0.1	6 ± 1	20.3 ± 1.5
Viper	0.01	36 ± 6	1.3 ± 0.1	15 ± 5	12.3 ± 1.5
	0.1	37 ± 8	1.3 ± 0.2	12 ± 4	12.6 ± 2.1
	1	37 ± 3	1.3 ± 0.05	4 ± 1	20.3 ± 1.5

3.1.2. Wire cutting tests

Wire-cutting tests were performed to determine the Griffith critical energy release rate (G_c). The average cutting force values were determined from the force-insertion curves. These values were divided by the corresponding breadth of the gel block and are plotted against the diameter of the corresponding wire diameters. A straight line is fit to the data points using the

212 equation below [15] and the intercept of the line-fit represents the Griffith critical energy
213 release rate (Fig. 6).

214
$$\left(\frac{F}{B}\right) = (1 + \mu)\sigma d + G_c \qquad (1)$$

215 where,

216 B = sample width, μ = kinematic friction coefficient, σ = characteristic stress, and G_c =
217 Griffith critical energy release rate. From the fit, we estimate the values of G_c to be 0.245
218 J/m^2. Using this value of G_c and the average Young's modulus ($E \approx 380$ kPa) determined
219 from the compression experiments and the Poisson's ratio ($\upsilon \approx 0.3$), we estimate the stress
220 intensity factor (K_c) using:

221
$$K_c = \sqrt{G_c \frac{E}{1-\upsilon^2}} \qquad (2)$$

222 Thus, we get $K_c \approx 0.33$ kPa√m.
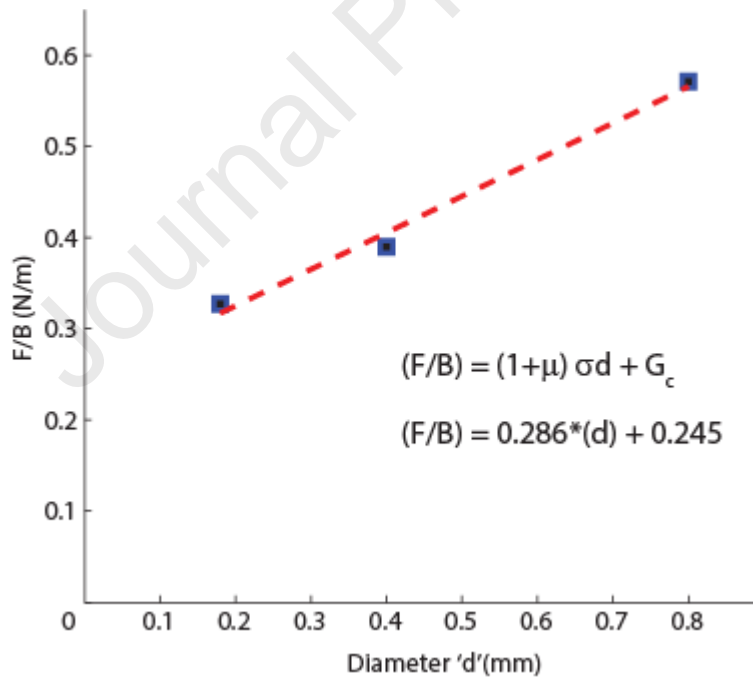
223

224 **Figure 6**. Wire cutting test results from three different diameter wires.

225 **3.2. Modelling**

226 Modelling of the fang-gel interaction was done in three parts. The first part of interaction is
227 the indentation of the gel surface without any insertion (Figure 7, A). The second part of
228 interaction includes sudden piercing of the gel (Figure 7, B), followed by the third interaction

229   that is the continuous insertion of fang into the gel (Figure 7, C). As the fang is pushed more
230   into the gel, there is an increase in the recorded force because of the compression of higher
231   gel volume as a result of the increase in the diameter of the fang from tip to the base. In
232   contrast, the experimental results based on cylindrical needles, the insertion force is almost
233   constant after piercing because of the constant diameter [9,16]. We approximate the fangs as
234   cones and assume the substrate as a linear elastic material to perform modelling of insertion
235   force curve.

236   Since we are using the insertion equation to model also the fracture part, here we will discuss
237   first the indentation and insertion phenomena.
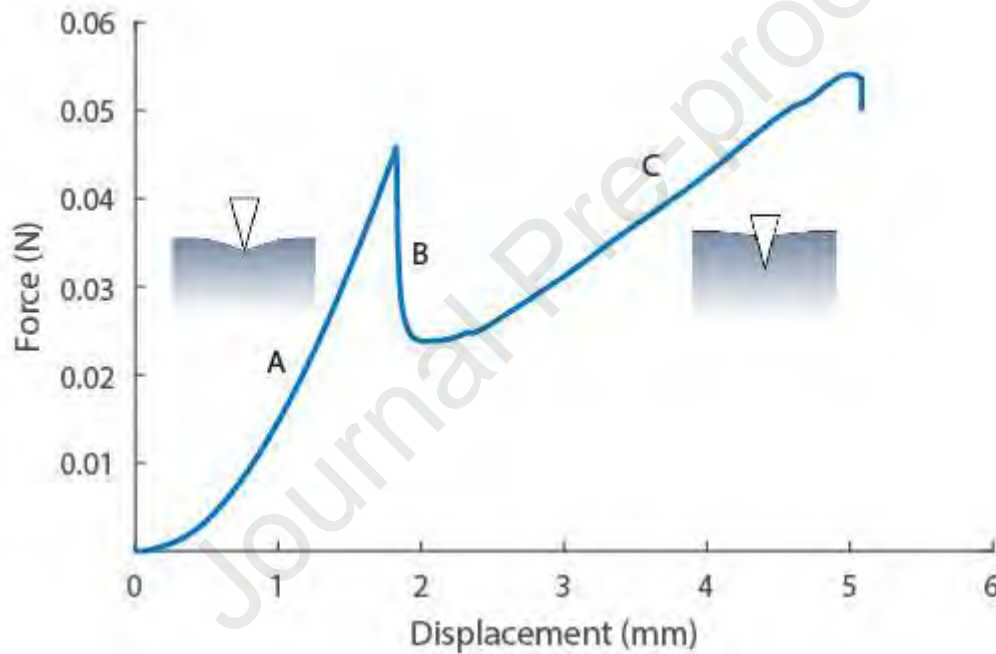
238

239   **Figure 7.** Force-displacement curve with a schematic view of the indentation (left, A) and
240   insertion (right, C) mechanisms. (Example data for the viper fang, $s = 0.1$ mm/s, test no. 1).

241

242   **3.2.1. Indentation**

243   The initial interaction of the fang and gel is modelled as a non-adhesive and frictionless
244   indentation of an elastic half-space by a rigid cone-shaped indenter as shown in Figure 8A.
245   The derived relationship between insertion depth (δ), contact radius (a) and indenter half
246   cone angle (β) can be written as [17]:

247   $$\delta = \frac{\pi}{2} \frac{a}{\tan \beta} \tag{3}$$

248   The corresponding indentation force F_i is given by:

249     $$F_i(\delta) = \frac{2\,E}{1-v^2}\,a\,\left(\delta - \frac{\pi\,a}{4\,\tan\beta}\right) = \frac{2\,E}{1-v^2}\,\frac{\tan\beta}{\pi}\,\delta^2 \qquad (4)$$

250   where E is the Young's modulus and v is the Poisson's ratio of the substrate. We employ

251   equation (4) to fit the experimental data of the indentation part of the curves, by assuming $v =$

252   0.5 for the gelatin [18] and the experimental value $E = 380$ kPa, measured independently as

253   reported above. The results of the fits allow us to determine the equivalent half cone angles of

254   the fangs, i.e., $\beta = 3.4\pm0.4°$ for the viper fang and $\beta = 2.5\pm0.4°$ for the burrowing snake fang.

255   These results are in reasonable agreement with the optical measurements of the fangs shown

256   in Figure 8B, suggesting that the equivalent angles are nearly half of the macroscopic

257   geometrical ones and therefore, even more efficient shape of the fangs. The deformed shape

258   of the surface outside of the contact area (i.e., for $x > a$) is given by [17]:

259     $$u(x) = \frac{2\,\delta}{\pi\,a}\left[a\,\sin^{-1}\left(\frac{a}{x}\right) - x + \sqrt{x^2 - a^2}\right] \qquad (5)$$

260   Some earlier studies in the literature make use of a two-term equation for fitting indentation

261   data, i.e. [9,16]:

262     $$F_i(\delta) = A\,\delta^2 + B\,\delta \qquad (6)$$

263   where A and B are fitting parameters. Although we are not providing an analytical derivation

264   of this additional term, it might be related to one or more of the introduced approximations,

265   i.e., the nonlinear elasticity of the material and the geometry of the fang. The differences are

266   observed between the values of experiments and modelling primarily because of the

267   assumption that fang tips are perfect cones. The results do not appear to be strongly affected

268   by the velocity; instead, the effect of fang-shape is more relevant, given the lower values of

269   modulus for the burrowing snake fang.

270

271 Viper (*Bitis arietans*)   Burrower (*Atractaspis aterrima*)
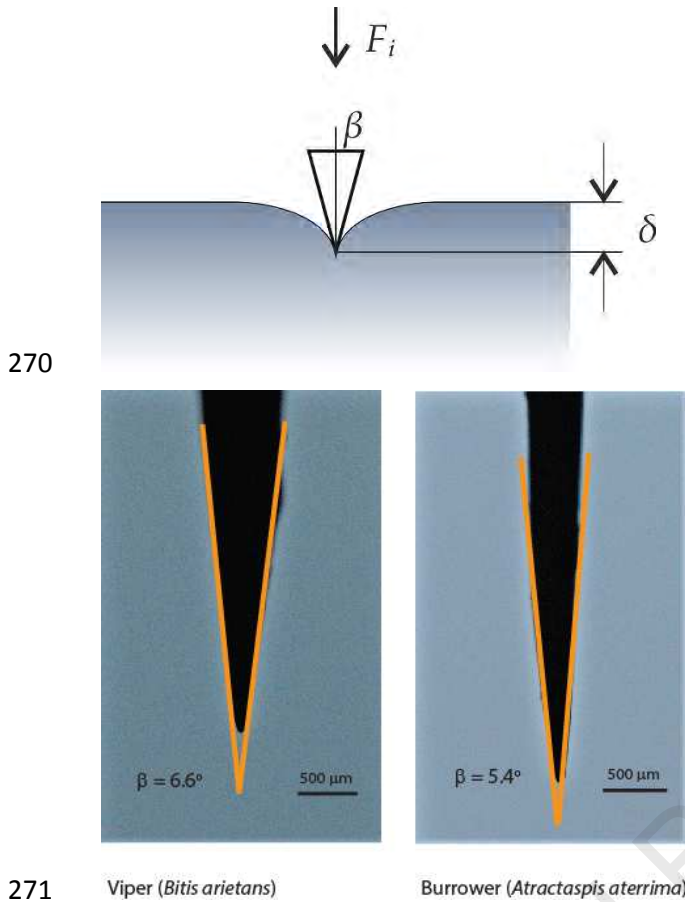
272 **A.**   **B.**

273 **Figure 8A.** Schematic view of the indentation process, as described in Equations (3,4). **B.**

274 Viper (left) and Burrowing snake (right) fangs and extracted cone angles.

275

276

277 **3.2.2. Insertion**

278 The insertion part of the curves is modelled by considering the fracture propagation and the

279 strain energy developed during the progressive piercing. The mechanics of insertion into a

280 soft substrate is driven by the work required to create a unit surface of the crack dW_{crack} and

281 the stored strain energy per unit volume dU_{strain} [8]. Thus, the insertion work expended by the

282 tip must balance the sum of dW_{crack} and dU_{strain}:

283
$$F_{p,0}\, d\delta = dW_{crack} + dU_{strain} \tag{7}$$

284 where $F_{p,0}$ is the insertion force. The infinitesimal lateral area changes of the cone penetrating

285 the substrate of an infinitesimal displacement $d\delta$ is given by:

286
$$dA = \pi \, (r + r + dr) \, dl \approx 2\pi \frac{\tan \beta}{\cos \beta} \, \delta \, d\delta \qquad (8a)$$

287 where we have neglected the high-order terms, and used the expressions for radius, $r =$
288 $\delta \tan \beta$ and cone length, $l = \delta/\cos \beta$. In the volume-related term of Equation (7), i.e. the
289 strain energy, we assume that the stresses arising from the insertion process involve a
290 spherical area around the tip, with radius equal to the insertion depth δ. Therefore, we get:

291
$$dV = 4\pi \, \delta^2 \, d\delta \qquad (8b)$$

292 Here we assume that during insertion there is a stable crack propagation and the crack
293 maintains a conical shape. Thus, the work required to create an incremental opening of the
294 crack must equal the critical strain energy release rate [8], which, for a mode-I crack opening,
295 is related to the material fracture toughness $K_{\mathrm{I}c}$ through:

296
$$G_{\mathrm{I}c} = \frac{1 - \nu^2}{E} \, K_{\mathrm{I}c}^2 \qquad (9)$$

297 valid for plane-strain conditions. Therefore, by making use of Equation (8a), we get:

298
$$dW_{\mathrm{crack}} = G_{\mathrm{I}c} \, dA \approx 2\pi \frac{\tan \beta}{\cos \beta} \frac{1 - \nu^2}{E} \, K_{\mathrm{I}c}^2 \, \delta \, d\delta \qquad (10)$$

299 The strain energy, considering the involved volume from Equation (8b), is given by:

300
$$dU_{\mathrm{strain}} \approx \frac{1}{2} \frac{1 - \nu^2}{E} \, \sigma^2 \, dV \approx 2\pi \frac{1 - \nu^2}{E} \, \sigma^2 \, \delta^2 \, d\delta \qquad (11)$$

301 where σ can be assumed to be an average stress around the tip during insertion and, again, the
302 plane-strain Young's modulus is employed.

303 Finally, we can insert Equations (10) and (11) into Equation (7), to obtain:

304
$$F_{p,0} \, d\delta \approx 2\pi \frac{\tan \beta}{\cos \beta} \frac{1 - \nu^2}{E} \, K_{\mathrm{I}c}^2 \, \delta \, d\delta + 2\pi \frac{1 - \nu^2}{E} \, \sigma^2 \, \delta^2 \, d\delta \qquad (12)$$

305 Since Equation (12) must hold for any $d\delta$, the force-displacement relationship during
306 insertion is:

307
$$F_{p,0}(\delta) \approx 2\pi \frac{\tan \beta}{\cos \beta} \frac{1 - \nu^2}{E} \, K_{\mathrm{I}c}^2 \, \delta + 2\pi \frac{1 - \nu^2}{E} \, \sigma^2 \, \delta^2 \qquad (13a)$$

308 Equation (13a) is obtained by considering the surface of the substrate as flat. Due to friction,
309 this does not happen in experiments, thus the substrate surface remains deflected of a small

310   quantity $\alpha\,\delta_{cr}$, with $\alpha < 1$ and δ_{cr} is the critical displacement related to fracture. This effect

311   can be considered, as shown in Figure 9, by:

312   •   considering the effective insertion depth, i.e. applying the change of variable $\delta \to \delta -$

313        $\alpha\delta_{cr}$;

314   •   adding a term due to the indentation of the substrate (up to a depth $\alpha\,\delta_{cr}$), as the

315   indentation by an equivalent rigid flat punch of radius a_{cr}, assumed to be constant in a

316   first approximation. This assumption is reasonable considering that, after the initial quasi-

317   conical shape, the diameter of the fangs becomes almost constant (Figure 8B).

318   Accordingly, Equation (13a) modifies as follows:

319     $F_p(\delta) \approx \pi \frac{\beta}{\cos\beta} \frac{1-\nu^2}{E} K_{\mathrm{Ic}}^2 (\delta - \alpha\,\delta_{cr}) + 2\pi \frac{1-\nu^2}{E} \sigma^2 (\delta - \alpha\,\delta_{cr})^2 + \frac{4}{\pi}\tan^2\beta\;\delta_{cr}^2\,p_{eq}$ (13b)

320   where p_{eq} is an equivalent pressure related to the flat punch indentation described above,

321   acting on the area $\pi\,a_{cr}^2$, and a_{cr} related to δ_{cr} through Equation (3). The result can be

322   considered a measure of the effect of friction and/or adhesion between the fang and the

323   substrate. Rearranging and neglecting high-order terms (i.e. assuming $\alpha^2 \ll 1$), we get:

324                                    $F_p(\delta) \approx A\,\delta^2 + B\,\delta + C$ (14)

325   with:

$$
\begin{cases}
A = 2\pi \dfrac{1-\nu^2}{E}\,\sigma^2 \\[2mm]
B = 2\pi \dfrac{\tan\beta}{\cos\beta} \dfrac{1-\nu^2}{E} K_{\mathrm{Ic}}^2 - \alpha\,\delta_{cr}\,4\pi \dfrac{1-\nu^2}{E}\,\sigma^2 \\[2mm]
C = \dfrac{4}{\pi}\tan^2\beta\;\delta_{cr}^2\,p_{eq} - 2\pi\,\alpha\,\delta_{cr} \dfrac{\tan\beta}{\cos\beta} \dfrac{1-\nu^2}{E} K_{\mathrm{Ic}}^2
\end{cases}
$$

326   The experimental data was fit to Equation (14) to estimate the average stress during insertion

327   σ and the equivalent pressure p_{eq}, as listed in Table 3. The values of the Young's modulus and

328   of the fracture toughness of the material, instead, are taken from the experimental

329   measurements reported in Section 3.2.1. Finally, we have chosen $\alpha \approx 0.1$, from experimental

330   observations.

331   We find values of stresses (namely, σ and p_{eq}) that are almost independent on the insertion

332   speed (v), but rather they are different between the two considered geometries. Interestingly,

333   we observe that the fang of the burrowing snake presents lower values of stress during

334 insertion (σ): this can be seen as a more optimal insertion mechanism, due to the different

335 fang geometry with respect to the viper's fang.

336

337 A.   B.
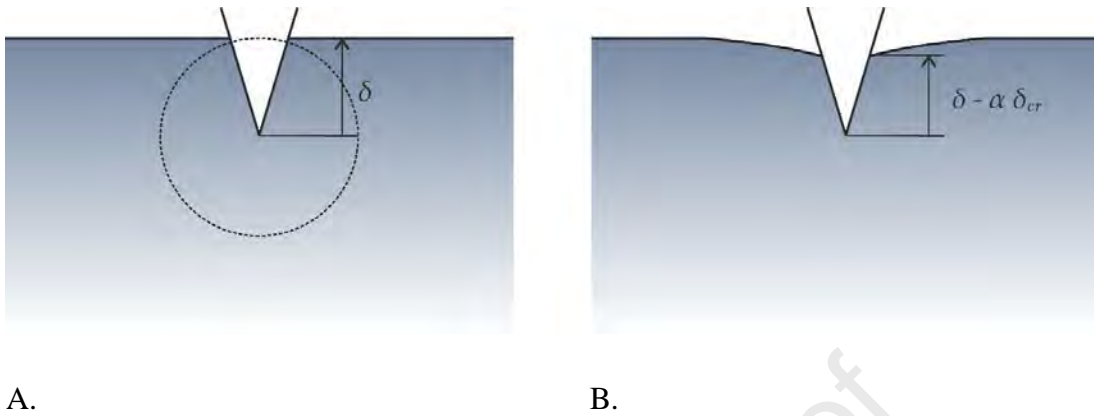
338 **Figure 9A.** Geometry during penetration with spherical volume considered for the strain

339 energy in Equation (11) **B**. effective penetration depth with substrate surface deflection.

340

341 **Table 3.** Estimated values of various parameters obtained from the fitting of the indentation

342 and insertion parts of the experimental curves.

343

sample	Insertion speed (v) (mm/s)	σ (kPa) from Equation (14)	p_{eq} (kPa) from Equation (14)
viper	0.01	11.0 ± 0.5	2200.0 ± 156.7
viper	0.1	11.7 ± 1.0	2447.1 ± 474.6
viper	1	10.2 ± 0.8	4247.3 ± 163.1
burrowing snake	0.01	10.7 ± 0.7	3733.7 ± 1397.8
burrowing snake	0.1	9.4 ± 0.1	4063.6 ± 647.8
burrowing snake	1	9.5 ± 0.3	4754.1 ± 188.0

344

3.2.3. Fracture

346 The fracture part of the force-displacement curves is characterised by an instantaneous drop

347 in the force, due to the initial crack formation. We estimate this force drop by making use of

348 the Equations (4) and (14), related to the indentation and insertion part, respectively. In order

349 to employ a formulation of the same type of Equation (14), we introduce the (empirical)

350 dimensionless coefficient $\eta \geq 1$, which multiplies the volume-dependent term in the

351 expression of the insertion force (i.e. the term related to strain energy). It is, in other words, a

352 measure to introduce the fracture phenomenon, happening for $\delta = \delta_{cr}$. Thus, we get the

353 following semi-analytical expression:

354
$$F'_p(\delta) \approx A\,\delta^2\,\eta + B\,\delta + C \tag{15}$$

355 which reduces to Equation (14) for $\eta = 1$.

356 Thus, it is possible to extract η from Equations (15) and (4) evaluated at $\delta = \delta_{cr}$ (this latter

357 quantity taken from the experimental data), obtaining:

358
$$\eta \approx \frac{\frac{2\,E}{1-\nu^2}\frac{\tan\beta}{\pi}\delta_{cr}^2 - B\,\delta_{cr} - C}{A\,\delta_{cr}^2} \tag{16}$$

359 Consequently, the corresponding force drop is found by subtracting Equation (14) from

360 Equation (15) at the critical displacement δ_{cr}:

361
$$\Delta F \approx A\,\delta_{cr}^2\,(\eta - 1) \tag{17}$$

362 The estimated values of force drop are very close to those observed in the experiments (Table

363 4), confirming the good quantitative performance of the proposed model. The observed

364 differences between the model estimations and experimental values can be attributed to the

365 introduced assumptions on material and geometry, as already discussed in the derivation of

366 the indentation and insertion laws.

367 **Table 4.** Estimated values of the force drop ΔF and comparison with experiments.

Sample	Insertion speed (v) (mm/s)	Force drop (model) (mN)	Force drop (experiments) (mN)
Viper	0.01	19 ± 2	24 ± 4
	0.1	18 ± 7	22 ± 4
	1	1 ± 1	6 ± 1
Burrowing snake	0.01	11 ± 6	15 ± 5
	0.1	9 ± 3	12 ± 4
	1	4 ± 1	4 ± 1

368

4. Conclusions

We compared mechanical properties of fangs of two snake species with different sizes and their also piercing process using gelatine hydrogels. The fangs of both the species appear to have similar mechanical properties but there was a difference in the insertion forces owing to the difference in their shape. Our analytical modelling results show that we are able to model the interaction between the fang and the substrate, obtaining a good agreement with the experimental evidence. Despite we have introduced some simplifying assumptions, we have been able to provide interesting insights into fang insertion mechanisms, highlighting the smaller values of stresses, and thus a higher efficiency, associated with the insertion of the burrowing snake's fang. Our findings may aid in understanding mechanics and design of bioinspired surgical needles into soft materials such as human skin.

References

1. Meyers MA, McKittrick J, Chen P-Y. 2013 Structural biological materials: critical mechanics-materials connections. *Science* **339**, 773–9. (doi:10.1126/science.1220854)

2. Jackson K. 2002 How tubular venom-conducting fangs are formed. *J. Morphol.* **252**, 291–297. (doi:10.1002/jmor.1106)

3. Zahradnicek O, Horacek I, Tucker AS. 2008 Viperous fangs: Development and evolution of the venom canal. *Mech. Dev.* **125**, 786–796. (doi:10.1016/j.mod.2008.06.008)

4. Jackson K. 2003 The evolution of venom-delivery systems in snakes. *Zool. J. Linn.*

397   *Soc.* **137**, 337–354. (doi:10.1046/j.1096-3642.2003.00052.x)

398   5.   Politi Y, Priewasser M, Pippel E, Zaslansky P, Hartmann J, Siegel S, Li C, Barth FG,
399   Fratzl P. 2012 A spider's fang: How to design an injection needle using chitin-based
400   composite material. *Adv. Funct. Mater.* **22**, 2519–2528.
401   (doi:10.1002/adfm.201200063)

402   6.   Kardong K V. 2016 'Protovipers' and the Evolution of Snake Fangs Author(s):
403   Kenneth V. Kardong Source: **33**, 433–443.

404   7.   O'Leary MD, Simone C, Washio T, Yoshinaka K, Okamura a. M. 2003 Robotic
405   needle insertion: effects of friction and needle geometry. *2003 IEEE Int. Conf. Robot.*
406   *Autom. (Cat. No.03CH37422)* **2**, 1774–1780. (doi:10.1109/ROBOT.2003.1241851)

407   8.   Shergold O a., Fleck N a. 2004 Mechanisms of deep penetration of soft solids, with
408   application to the injection and wounding of skin. *Proc. R. Soc. A Math. Phys. Eng.*
409   *Sci.* **460**, 3037–3058. (doi:10.1098/rspa.2004.1315)

410   9.   Okamura AM, Simone C, O'Leary MD. 2004 Force modeling for needle insertion into
411   soft tissue. *IEEE Trans. Biomed. Eng.* **51**, 1707–1716.
412   (doi:10.1109/TBME.2004.831542)

413   10.   Matushkina N, Gorb S. 2007 Mechanical properties of the endophytic ovipositor in
414   damselflies (Zygoptera, Odonata) and their oviposition substrates. *Zoology (Jena).*
415   **110**, 167–75. (doi:10.1016/j.zool.2006.11.003)

416   11.   Zhao Z-L, Zhao H-P, Ma G-J, Wu C-W, Yang K, Feng X-Q. 2015 Structures,
417   properties, and functions of the stings of honey bees and paper wasps: a comparative
418   study. *Biol. Open* **4**, 921–928. (doi:10.1242/bio.012195)

419   12.   Cundall D. 2015 Viper fangs: functional limitations of extreme teeth. *Physiol.*
420   *Biochem. Zool.* **82**, 63–79. (doi:10.1086/594380)

421   13.   Abràmoff MD, Magalhães PJ. 2004 Image Processing with ImageJ. *Biophotonics Int.*

422   14.   Jansen van Vuuren L, Kieser JA, Dickenson M, Gordon KC, Fraser-Miller SJ. 2016
423   Chemical and mechanical properties of snake fangs. *J. Raman Spectrosc.* **47**, 787–795.
424   (doi:10.1002/jrs.4903)

425 15. Kamyab I, Chakrabarti S, Williams JG. 1998 Cutting cheese with wire. *J. Mater. Sci.*
426   **33**, 2763–2770. (doi:10.1023/A:1017517332112)

427 16. Mahvash M, Dupont PE. 2010 Mechanics of dynamic needle insertion into a biological
428   material. *IEEE Trans. Biomed. Eng.* **57**, 934–943. (doi:10.1109/TBME.2009.2036856)

429 17. Sneddon IN. 1965 The relation between load and penetration in the axisymmetric
430   boussinesq problem for a punch of arbitrary profile. *Int. J. Eng. Sci.* **3**, 47–57.
431   (doi:10.1016/0020-7225(65)90019-4)

432 18. Czerner M, Fellay LS, Suárez MP, Frontini PM, Fasce LA. 2015 Determination of
433   Elastic Modulus of Gelatin Gels by Indentation Experiments. *Procedia Mater. Sci.* **8**,
434   287–296. (doi:10.1016/j.mspro.2015.04.075)

435 19. K.L.Johnson. 1985 *Contact Mechanics*. Cambridge University Press.

436